Supporting Information

Lu Yang,[1,2] Zepeng Liu,[1,3] Shuwei Li,[1,3] Zhiwei Hu,[4] Qingyu Kong,[5,6] Xi Shen,[7] Qi Liu,[8] He Zhu,[8] Jin-Ming Chen,[9] Shu-Chih Haw,[9] Yurui Gao,[10] Yingying Wang,[7] Dong Su,[7] Xuefeng Wang,*[1,2,7] Richeng Yu,*[3,7] Zhaoxiang Wang,*[1,2,3] Liquan Chen[1]

[1] Key Laboratory for Renewable Energy, Chinese Academy of Sciences, Beijing Key Laboratory for New Energy Materials and Devices, Institute of Physics, Chinese Academy of Sciences, Beijing 100190, China

[2] College of Material Science and Opto-Electronic Technology, University of Chinese Academy of Sciences, Beijing 100049, China

[3] School of Physical Sciences, University of Chinese Academy of Sciences, Beijing 100049, China

[4] Max Planck Institute for Chemical Physics of Solids, Dresden 01187, Germany

[5] Synchrotron Soleil L'Orme des Merisiers St-Aubin Gif-sur-Yvette Cedex 91192, France

[6] School of Physical Science and Information Technology, Liaocheng University, Liaocheng 252059, China

[7] Laboratory for Advanced Materials and Electron Microscopy, Institute of Physics, Chinese Academy of Sciences, Beijing 100190, China

[8] Department of Physics, City University of Hong Kong, Hong Kong 999077, China

[9] National Synchrotron Radiation Research Center, Hsinchu 30076, Taiwan

[10] Laboratory of Theoretical and Computational Nanoscience, CAS Key Laboratory for Nanosystem and Hierarchy Fabrication, CAS Center for Excellence in Nanoscience, National Center for Nanoscience and Technology, Chinese Academy of Sciences, Beijing 100190, China

* Corresponding Authors: Zhaoxiang Wang (zxwang@iphy.ac.cn); Xuefeng Wang (wxf@iphy.ac.cn); Richeng Yu (rcyu@iphy.ac.cn);

Experimental Section

1. Material Synthesis

Preparation of the sodium salt precursor: $Na_2Mn_3O_7$ was synthesized by a solid-state reaction from stoichiometric amount of MnO_2 and NaOH (Alfa Aesar Co.). The above materials were mixed using a mortar and pestle in the infrared lamp, and then the mixed precursor materials were annealed at 450℃ for 24 h in air condition. The obtained $Na_2Mn_3O_7$ was collected at room temperature and stored in the Ar-filled glove-box (Mbraun Co.).

Preparation of the $Fd\bar{3}m$ $Li_2Mn_3O_{7-x}$: The obtained $Na_2Mn_3O_7$ was subjected to ion-exchange in molten $LiNO_3$/LiCl (88:12 w/w) at 280°C for 4 h.[1] Then the mixtures were washed with deionized water several times, and dried at 110°C for 10 h. Finally, the prepared $Li_2Mn_3O_{7-x}$ was stored in the Ar-filled glove-box to avoid the reaction with H_2O and CO_2.

2. Electrochemical Measurements

The cathode sheets were prepared by mixing the active material (70wt.%), carbon black (20wt.%) and polyvinylidene fluoride (PVDF) (10wt.%) dissolved in *N*-methyl pyrrolidone (NMP). The slurry was then cast onto a carbon-coated aluminum (Al) foil. The cathode sheets were dried at 120°C for 6 h in a vacuum oven. The loading of the active material was 4~5 mg cm^{-2} in the cells for the following *in situ* XRD test but ~2 mg cm^{-2} in the cells for the other purposes. Coin cells were assembled with fresh Li foil as the counter electrode, and LB111 (Duoduo Co.) as the electrolyte in an Ar-filled glovebox. The performance evaluation and the electrochemical treatment of the active material were carried out on a Land CT2001A battery test system (Wuhan, China) at room temperature (25°C).

3. Material Characterization

3.1 XRD and ICP

The morphology of the sample was observed on a scanning electron microscope (Hitachi S-4800). The XRD patterns were recorded between 10° and 80° (2 theta) using the Cu Kα (λ=1.54 Å) radiation on a D8 Bruker Advanced X-ray diffractometer. The Rietveld refinement of the XRD pattern was carried out using the GSAS program. The actual content of the element in the final sample was determined by inductively coupled plasma-atomic emission spectroscopy (ICP-AES; Shimadzu, ICPS-8100). In order to reduce the interference of ionization, the three kinds of mixed standard solutions (Li, Na, and Mn elements) with different concentrations were prepared, and a standard curve was plotted. Then the ICP-AES of experimental samples were tested according to the standard profiles.

3.2 TEM and STEM Imaging

The structures of $Li_2Mn_3O_{7-x}$ was characterized using an ARM-200F (JEOL, Tokyo, Japan) transmission electron microscope (TEM) operated at 200 kV and equipped with double spherical aberration (Cs) correctors. The attainable resolution is 78 picometers.

3.3 X-ray Absorption Spectroscopy

The soft X-ray absorption spectroscopy (XAS) measurements at the O *K*-edges were carried out in both total electron yield (TEY) and total fluorescence yield (TFY) modes and at the Mn L_3-edge in the TEY mode at the Beamline (BL) 11A of the National Synchrotron Radiation Research Center (NSRRC), Taiwan. In addition, the bulk-sensitive inverse partial fluorescence yield (IPFY) spectra at the Mn L_3-edge were measured using a silicon drift detector with an energy-resolution of ~120 eV at BL 20A1 at NSRRC. All the samples were transferred under proper protections in any of the above tests.

The X-ray absorption near edge structure (XANES) and extended X-ray absorption fine structure (EXAFS) spectra of the Mn *K*-edge were collected at ODE and ROCK beamline of the SOLEIL synchrotron in France. The Athena and Artemis programs in Ifeffit software package was used to process

the XANES and EXAFS data.[2]

4. DFT Methods

The calculations in the paper were performed through the Vienna *Ab initio* simulation package (VASP)[3] with the projector-augmented wave (PAW)[4] method. The generalized gradient approximation with Perdew-Burke-Ernzerhof (PBE)[5] exchange-correlation functional were selected for all the calculations. The energy cutoff for the plane waves was set to 520 eV for all the structures. A Γ-center 2 × 2 × 2 *k*-points mesh was used to integrate the Brillouin zone in the calculations. All the structures were fully relaxed until the energy convergence to 1×10^{-5} eV.

The structure parameter of $Li_2Mn_3O_{7-x}$ was determined according to the reference.[6] All the $Li_2Mn_3O_{7-x}$ structures were generated by supercell program and 15 random structures were selected for each type of $Li_2Mn_3O_{7-x}$ to reduce the error caused by different positions.

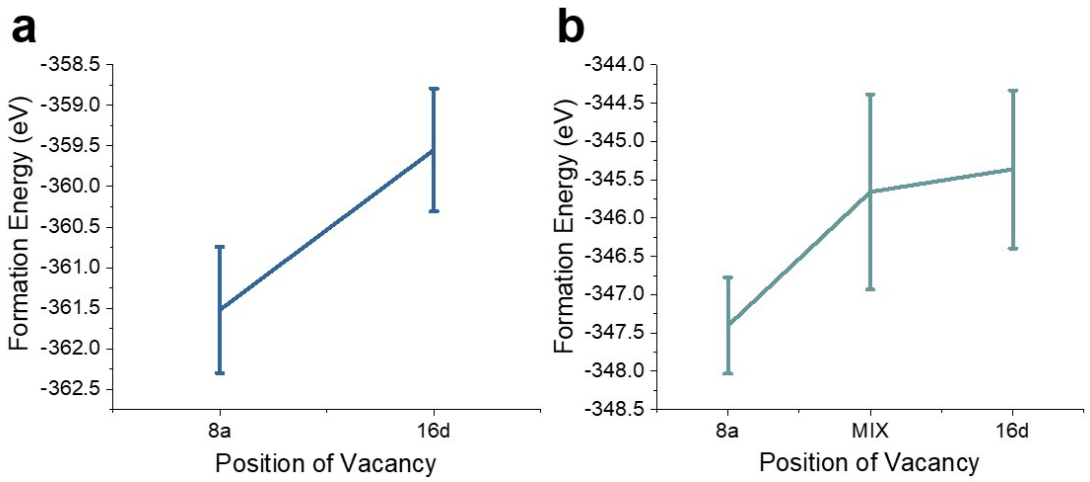

Figure S1. The DFT calculations of the formation energy of native vacancy in the tetrahedral, octahedral site or mixing site.

No sodium was detected with the ICP-AES in the ion-exchanged sample, indicating that all the Na ions in $Na_{4/7}[Mn_{6/7}\square_{1/7}]O_2$ has been exchanged with the Li ions (Table S1). The Li:Mn molar ratio in LMO is 0.68. Fitting to the X-ray absorption spectroscopy (XAS) spectra shows that the average oxidation state of Mn is 3.9. Therefore, the chemical formula of the lithium-manganese oxide was written as $Li_2Mn_3O_{7-x}$, a $vacancy_{Metal}$-containing spinel.

DFT calculations were conducted to figure out the occupation of the Mn vacancy (Figure S1). Since the vacancy can be located on the 8a site or the 16d site or both, three types of $Li_2Mn_3O_{7-x}$ were generated by a supercell program, named as LMO-8a, LMO-16d and LMO-mix, respectively, according to the occupation of their Mn vacancies.[35] Figure S1 shows the average total energy of the various possible occupancies in $Li_2Mn_3O_{7-x}$ and the corresponding error bar. The average total energy of LMO-8a is lower than that of the other two types of occupation. In addition, its error bar is also lower than the other two structures, indicating that the correlation between the energy and cation/vacancy distribution is weak in LMO-8a. Therefore, the vacancies are believed to occupy the 8a site.

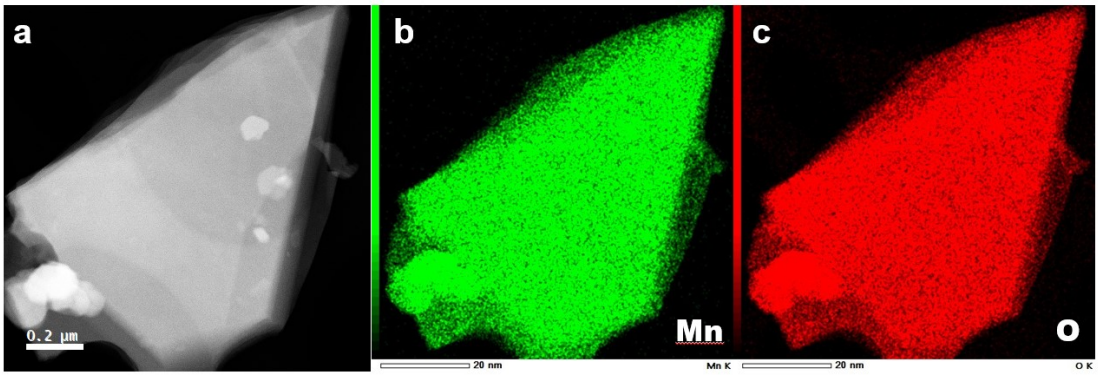

Figure S2. The STEM-EDS mapping images for Mn and O in spinel LMO.

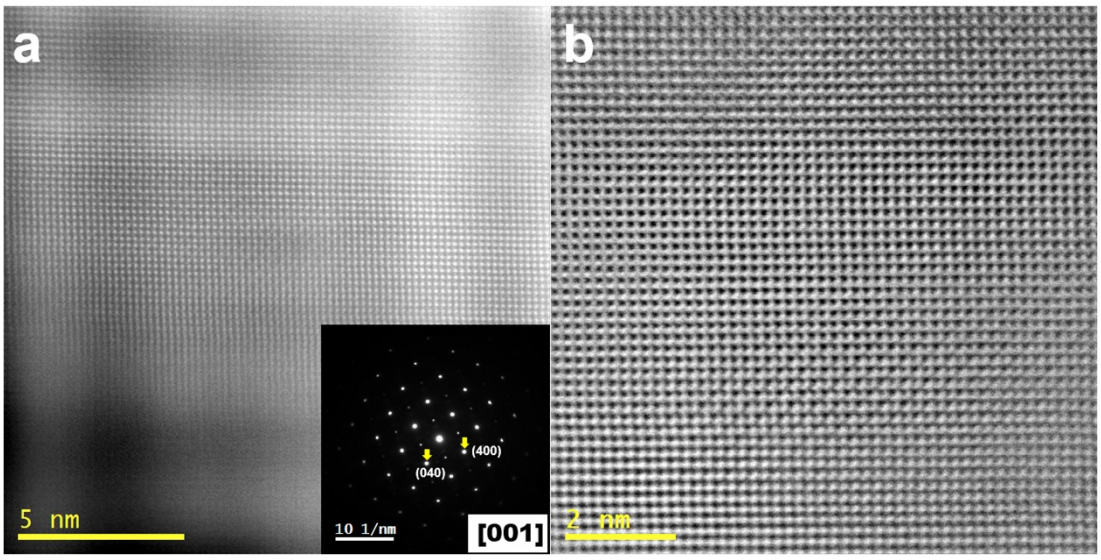

Figure S3. The HAADF (a) and ABF (b) images of LMO along the [001] zone axis. The inset in (a) is for the STEM-selected area electron diffraction (SAED) patterns of the as-prepared LMO.

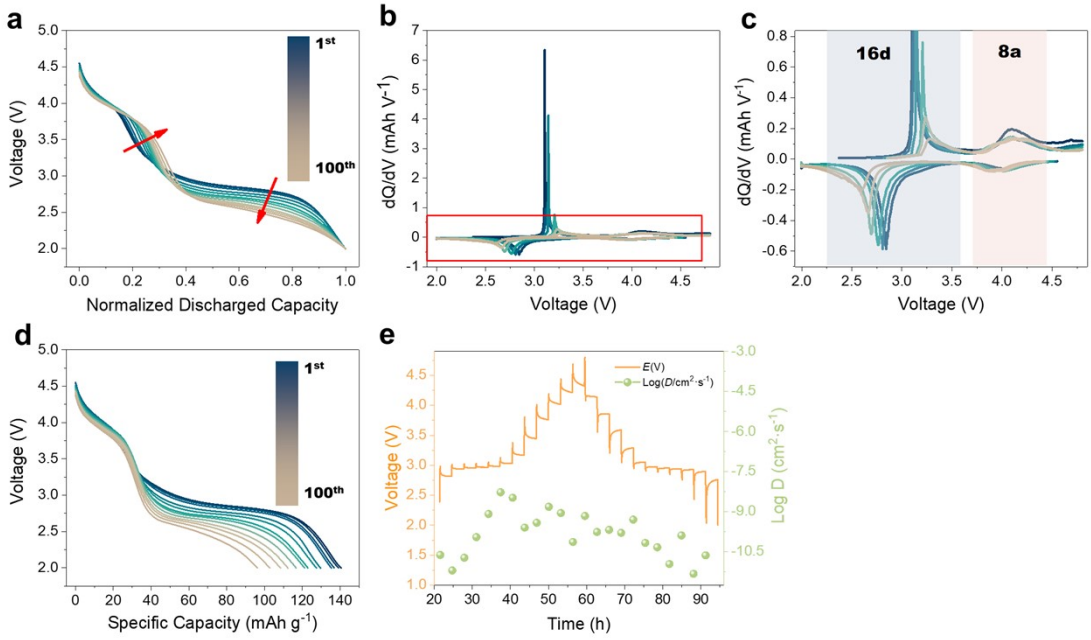

Figure S4. The normalized discharge capacity profiles of LMO between 2.0 V and 4.8 V (a), the dQ/dV discharge profiles (b), the magnified images (c) of the red rectangle in (b), the discharge profiles of LMO (d), the GITT profiles of LMO between 2.0 V and 4.8 V in the second cycle (e).

The normalized discharge profile (Figure S4a) indicates that the discharge voltage rises obviously above 3.0 V while the discharge voltage drops below 3.0 V, indicating that the voltage dropping below 3.0 V is responsible for the decay of the average discharge voltage in this process. The variation of the peak around 4.0 V is negligible in the dQ/dV profile in 100 cycles (Figure S4b and c), probably implying that the presence of the native vacancies is favorable for enhancing the structural robustness upon the Li^+ insertion/extraction on the tetrahedral (8a) sites. Meanwhile, the intensity of the peaks around 3.0 V for the Li^+ insertion/extraction on the 16d sites decreases and the polarization increases from the 6^{th} to the 100^{th} cycles.

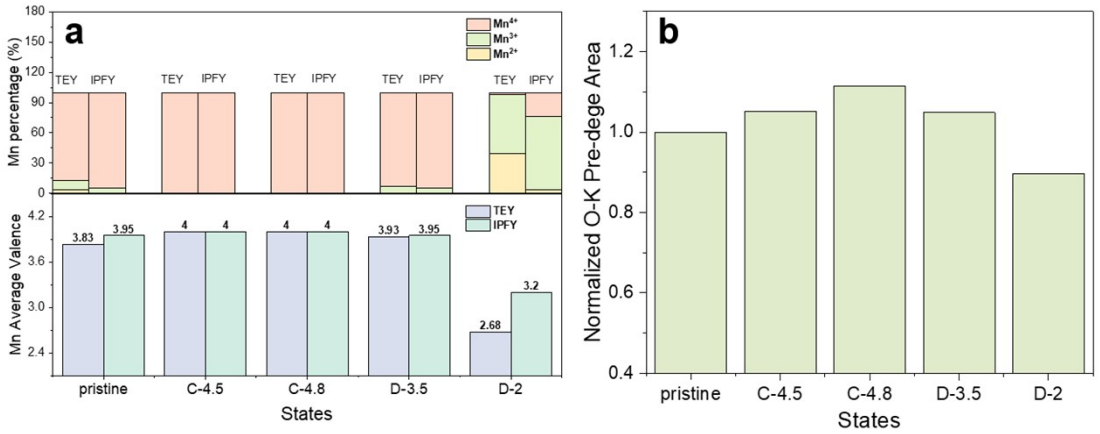

Figure S5. The results of fitting to the Mn L_3-edge spectra of samples at various states (a), the normalized intensity of O *K*-edge pre-edge area at different states of $Li_2Mn_3O_{7-x}$ in the TFY mode (b)

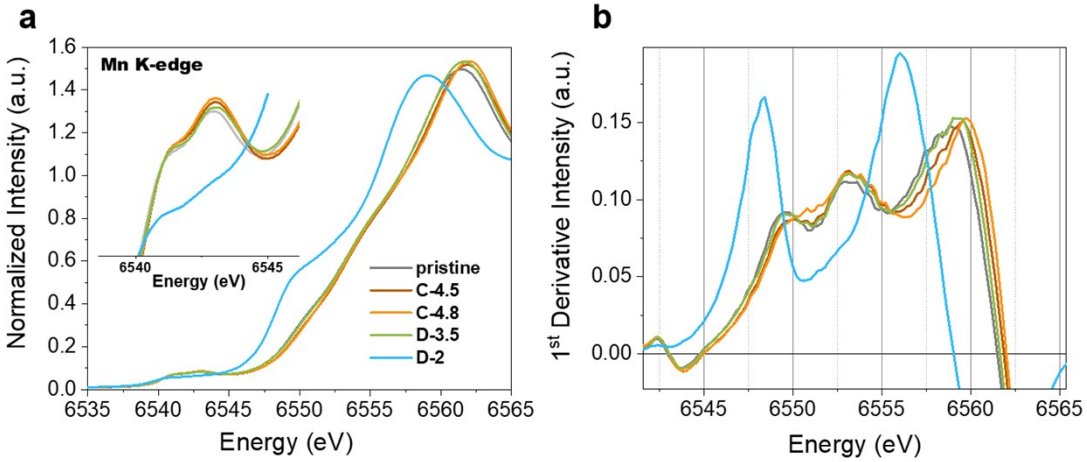

Figure S6. The Mn *K*-edge XANES spectra at different states (a, inset for the magnified Mn *K*-edge pre-edge peak), the 1st derivative spectra of Mn *K*-edge XANES spectra (b).

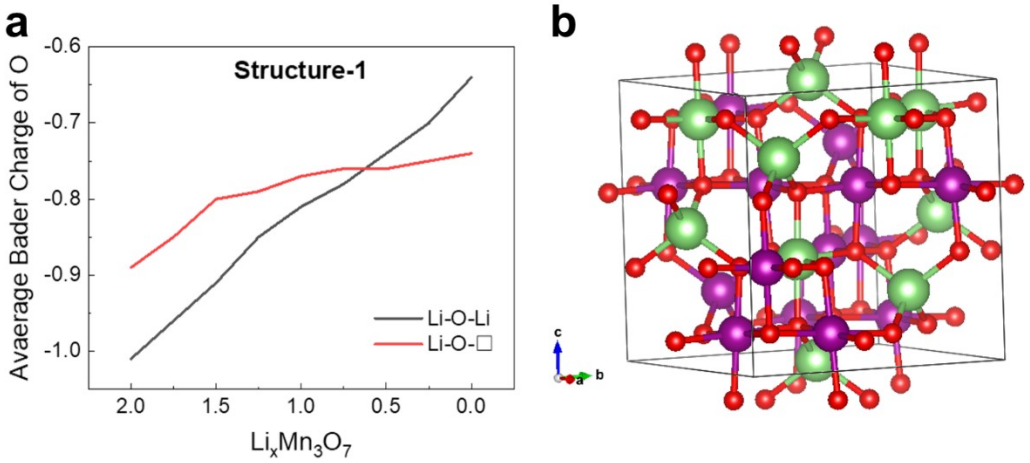

Figure S7. The average Bader charge of O on the different sites in $Li_xMn_3O_7$ (a) and the schematic structure diagrams (b) of $Li_xMn_3O_7$ for the DFT calculations.

The Bader charge analysis was conducted to compare the contribution of the O atoms in different environments to the charge compensation in $Li_2Mn_3O_7$ (Figure S7).[43] The average Bader charge (ABC) of O in the Li-O-Li structure increases faster than in the Li-O-□ structure, demonstrating that the oxygen in Li-O-Li provides more charge than the oxygen in Li-O-□ does during delithiation (-1.04 *vs.* -0.92 electrons per atom). We calculated the density of states of O in spinel $Li_2Mn_3O_7$ ($[Li_{4/7}Mn_{2/7}□_{1/7}]_{8a}[Li_{4/7}Mn_{10/7}]_{16d}[O_4]_{32e}$) and spinel $Li_4Mn_5O_{12}$ ($[Li]_{8a}[Li_{1/3}Mn_{5/3}]_{16d}[O_4]_{32e}$) and compared the activity of O in the Li-O-□, Li-O-Li and Li-O-Mn configurations (Figure S8). It shows that the O atom in the Li-O-□ and Li-O-Li configurations is closer to the Fermi energy than in the Li-O-Mn configuration. The O 2p band center of Li-O-Li, Li-O-□ and Li-O-M is -2.25 eV, -2.48 eV and -2.88 eV, respectively. These demonstrate that both the vacancy and the abundant Li are responsible for the activation of the oxygen redox to provide the high capacity.

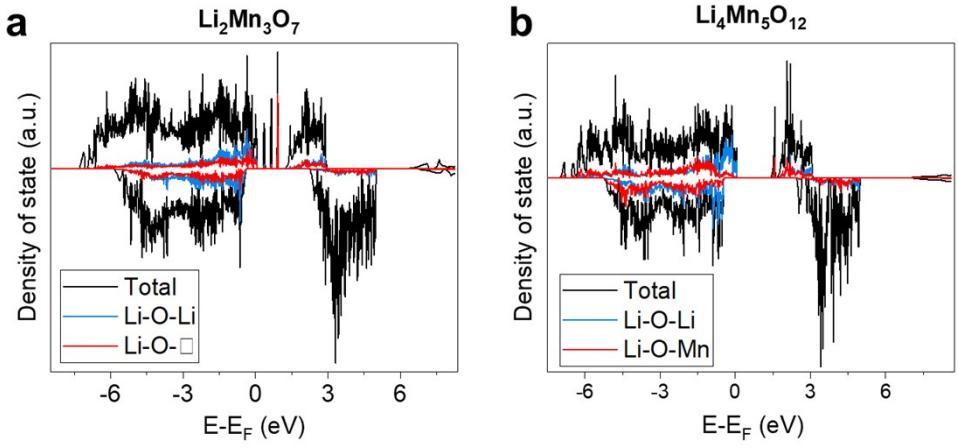

Figure S8. The density of states of O in spinel $Li_2Mn_3O_7$ (a) and spinel $Li_4Mn_5O_{12}$ (b).

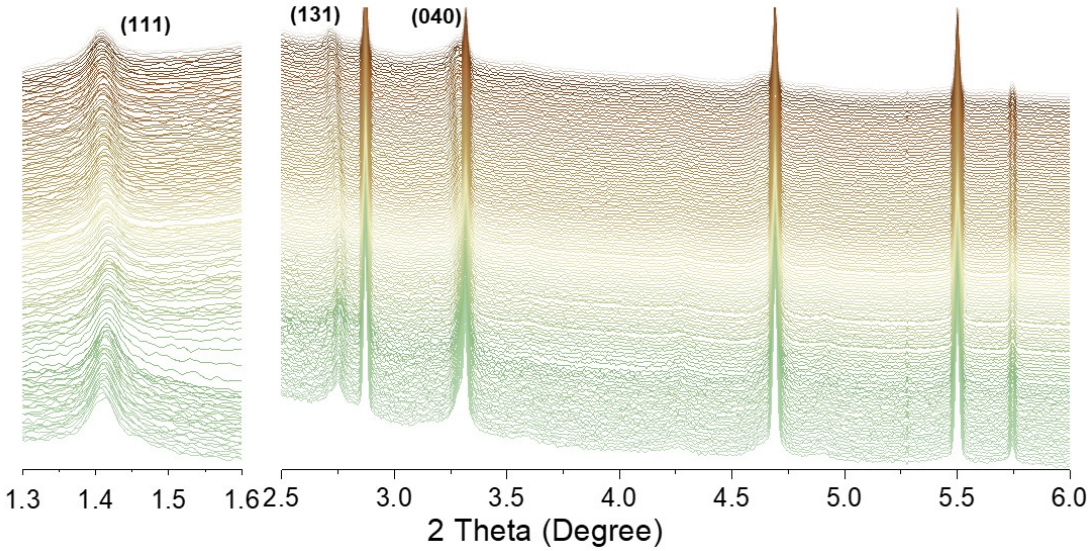

Figure S9. The *in situ* synchrotron XRD patterns (λ=0.1173 Å) of LMO in the first cycle between 2.0 V and 4.8 V at specific current of 20 mA g^{-1}.

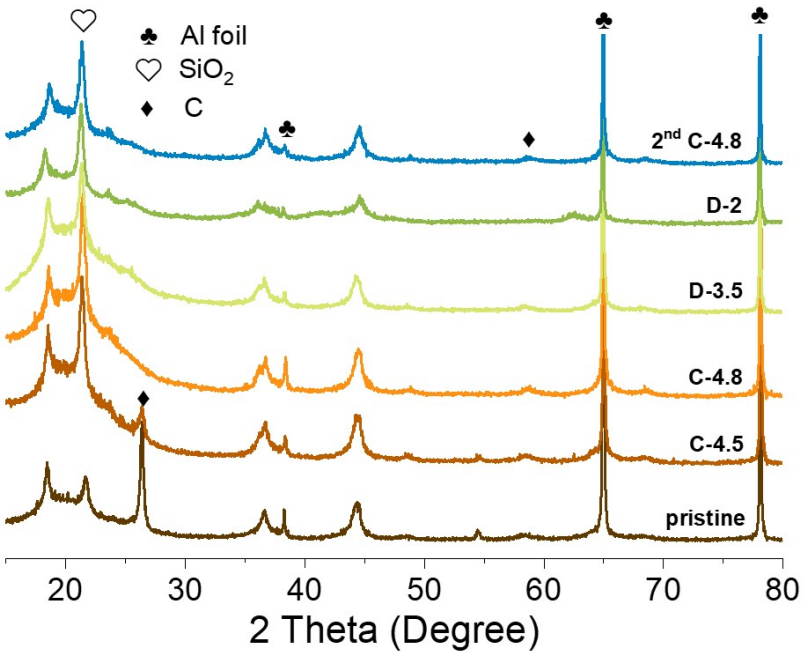

Figure S10. The XRD patterns (λ=1.54 Å) of LMO at different states (it took 1.5 h to collect a pattern).

Ex situ lab XRD (λ=1.54 Å, Figure S10) was also conducted to characterize the structural evolution. In order to reduce the experimental error, all the patterns were calibrated using the main peak of the Al current collectors at around 65°. The shifting of the main diffraction peak index is 0.13°. Thus, both the synchrotron and lab XRD tests demonstrate the zero-strain feature of the material and its similarity to its vacancy-containing maternal phase $Na_{4/7}[Mn_{6/7}\square_{1/7}]O_2$ ($Na_2Mn_3O_7$).[14] The presence of the vacancies in the spinel-structured materials makes the tetrahedron asymmetric and endows the structure with a more robust framework. According to the normalized discharge voltage profile and the dQ/dV profile, the insertion and extraction of the Li^+ ion on the 8a site is more reversible than that on the 16d site, indicating that the vacancy on the 8a site enhances the structural stability favorable for the reversible transmission of Li^+ ion.

Table S1. The ICP-AES results of $Na_{4/7}Mn_{6/7}\square_{1/7}O_2$ precursor and LMO.

sample	Li	Na	Mn
$Na_{4/7}Mn_{6/7}\square_{1/7}O_2$	-	0.68	1.00
After sample 1	0.68	0.01	1.00
After sample 2	0.68	0.01	1.00

Table S2. The refined crystallographic parameters by Rietveld analysis for LMO.

a=8.24688, b=8.24688, c=8.24688, α=90°, β=90°, γ=90°; Rwp=9.08%, GOF= 1.45, space group: $Fd\bar{3}m$					
Atom	***x***	***y***	***z***	**Occ.**	**Site**
Li1	0.1250	0.1250	0.1250	0.5714	8a
Li2	0.5000	0.5000	0.5000	0.2858	16d
Mn1	0.5000	0.5000	0.5000	0.7142	16d
Mn2	0.1250	0.1250	0.1250	0.2857	8a
O	0.3882	0.3882	0.3882	1	32e

Reference

1. J. Song, B. Li, Y. Chen, Y. Zuo, F. Ning, H. Shang, G. Feng, N. Liu, C. Shen, X. Ai and D. Xia, *Advanced Materials*, 2020, **32**, 2000190-2000197.
2. B. Ravel and M. Newville, *Journal of Synchrotron Radiation*, 2005, **12**, 537-541.
3. G. Kresse and J. Furthmüller, *Computational Materials Science*, 1996, **6**, 15-50.
4. P. E. Blochl, *Phys Rev B Condens Matter*, 1994, **50**, 17953-17979.
5. J. P. Perdew, K. Burke and M. Ernzerhof, *Physical Review Letters*, 1996, **77**, 3865-3868.
6. T. Takada, E. Akiba, F. Izumi and B. C. J. J. o. S. S. C. Chakoumakos, 1997, **130**, 74-80.